Effects of size on the mechanical response of metallic glasses investigated through in situ TEM bending and compression experiments

Chen, C.Q.; Pei, Y.T.; Hosson, J.T.M. De

Published in:
Acta Materialia

DOI:
10.1016/j.actamat.2009.08.070

Publication date:
2010

Available online at www.sciencedirect.com
ScienceDirect
Acta Materialia 58 (2010) 189–200
Acta MATERIALIA
www.elsevier.com/locate/actamat

Effects of size on the mechanical response of metallic glasses investigated through in situ TEM bending and compression experiments

C.Q. Chen, Y.T. Pei, J.T.M. De Hosson *

Department of Applied Physics, Materials Innovation Institute (M2i), University of Groningen, Nijenborgh 4, 9747 AG Groningen, The Netherlands

Received 9 July 2009; received in revised form 28 August 2009; accepted 31 August 2009
Available online 8 October 2009

Abstract

Quantitative bending and compression tests on micropillars made of two different amorphous alloys, with tip diameters ranging from 93 to 645 nm, are performed in situ in a transmission electron microscope (TEM). Under microcompression each pillar shows an intermittent plastic flow accommodated by inhomogeneous shear banding. However, the individual shear banding events are strongly size-dependent, i.e. in larger pillars the deformation is controlled by nucleation of shear bands, but in smaller pillars it becomes propagation-controlled. On the other hand, the yield stress is essentially size-independent. Microbending tests show further advantages by amplifying size effects and minimizing artifacts. An interesting finding is that by microbending, a switch from highly inhomogeneous to fully homogeneous deformation is observed at an experimentally accessible size regime near 200 nm, whereas it is not accessible under microcompression, even at a sub-100 nm scale. These size effects are well interpreted by a micromechanical model, leading to a deformation map in the stress-size space. A physical picture of nanoscale shear localization process is also provided.

Keywords: Transmission electron microscopy (TEM); Amorphous metals; Mechanical properties

1. Introduction

Since its discovery in the 1960s in the form of ribbons and later as thick bulk materials in the 1990s, metallic glasses (MGs) have attracted considerable attention [1–7]. Despite the high yield strength, monolithic metallic glass suffers from highly localized shear deformation at ambient temperature and therefore exhibits very limited ductility [3,4,8–10]. Understanding and controlling shear localization, especially with respect to the process by which shear bands accumulate in a specific microscopic location and propagate, both spatially and temporally, are still some of the major tasks in the research of metallic glasses [9–12].

Study of the deformation behavior of small volume metallic glass is an interesting route for the exploration of shear localization in MGs. Therefore it has attracted rapidly increasing interest over recent years [5,13–23]. It also has practical significance on guiding the design of recently booming MG-based composites [24–27] or multilayers [28,29], as an attempt to improve the ductility without compromising the strength. Size effects also come into play in applications of MG-components-incorporated micro-/nano-electromechanical systems (MEMS/NEMS) [30]. Despite numerous studies, there is no general consensus regarding the strength and deformation mode at small-length scale. In fact, significant controversy exists since either a dramatic increase of yield strength with decreasing size [16,17,19], or even the opposite trend [21,20], has been reported. Regarding the deformation mode, although there are reports on the observation of homogeneous flow at length scales of ~400–100 nm [13,14,20], other research has shown that deformation still occurs in localized shear bands (SBs), equally as in their bulk counterpart [18,21–23].

These inconsistencies arise largely from several aspects related to the test method itself. Most of the experiments are ex situ compression tests of micropillars fabricated with

* Corresponding author. Tel.: +31 50 363 4898; fax: +31 50 363 4881.
E-mail address: j.t.m.de.hosson@rug.nl (J.T.M. De Hosson).

1359-6454/$36.00 © 2009 Acta Materialia Inc. Published by Elsevier Ltd. All rights reserved.
doi:10.1016/j.actamat.2009.08.070

a focused ion beam (FIB). The information obtained from the ex situ experiments is limited by either a lack of quantitative stress–strain information [13] or by the incapability of monitoring the evolving deformation structure [15–21]. Especially, tapering is inevitable for FIB milled pillars with diameters down to submicrometer scale. The tapering is not a real problem for testing crystalline pillars; however, it is critical for pillars of MGs as during compression highly localized SBs may preferentially nucleate at the corner of sample-plunger contact [14–23]. This affects not only SB nucleation but also makes stress analysis rather difficult. This is especially so for the ex situ experiments when the events in the stress–strain curve cannot be correlated to particular individual SBs. These effects become more serious with smaller pillars. Another obstacle to observing intrinsic size effects in microcompression experiments is the fact that it is not possible to fabricate small enough pillars using FIB, e.g. tens of nanometers or smaller, which may be essential for the size effect, if any, to become noticeable.

In this paper we present striking new results of quantitative in situ bending and compression tests of amorphous micropillars carried out inside a transmission electron microscope (TEM). Real time recording of both the load and structural response of the pillars under compression revealed a strongly size-dependent shear banding that accommodates intermittent flow. It is demonstrated that bending tests bear particular advantages over compression tests by amplifying size effects and minimizing artifacts. A more complete switching from fully shear banding to fully homogeneous flow in an experimentally accessible regime is brought forward by microbending tests.

2. Experimental

Micropillars were cut by FIB from two kinds of metallic glass ribbons, Cu-based $Cu_{47}Ti_{33}Zr_{11}Ni_6Sn_2Si_1$ and Zr-based $Zr_{50}Ti_{16.5}Cu_{15}Ni_{18.5}$ prepared by melt spinning. Their elastic moduli measured by nanoindentation are 106 and 92 GPa, respectively. The tensile fracture behavior of the former made into thin foils has been recently investigated in situ in TEM [5]. Free-standing microwedges of thickness around 2 μm were first made from the ribbons with electrochemical etching. An FEI Strata DB235 dual beam FIB-SEM system was then used to mill a series of rectangular beams on the microwedge and finally micropillars out of these beams at 30 kV, as shown in Fig. 1. A final polishing procedure using an exceptionally low current of 20 pA is used and confirmed to be effective in reducing the surface damage, and minimizing the tapering angle that is inevitable in the milling of pillars with diameter smaller than 1 μm. More than 40 pillars of tip diameters ranging from 93 to 645 nm were successfully fabricated. The pillars have a rather small taper angle between 2.0° and 3.5°, and importantly well-defined gauge lengths ranging from 1.2–2.0 μm and aspect ratios from 3 to 8. TEM observations confirmed the uniform amorphousness of the micropillars.

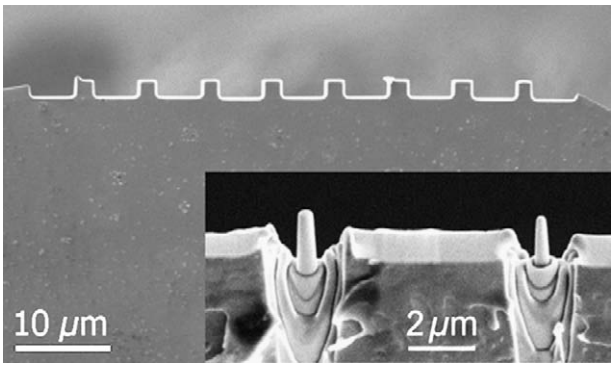

Fig. 1. MG pillars of submicrometer diameter fabricated through an optimized annular FIB milling procedure out of a wedge-shaped front of a ribbon thinned by electrochemical etching.

In situ TEM compression experiments were performed using a recently developed Hysitron picoindenter TEM holder (Hysitron Inc., Minneapolis, MN) equipped on a JEOL 2010F TEM, with a diamond flat punch 2 μm in diameter. A similar approach has been recently used in the investigation of the incipient plasticity of thin metallic films [31–34] and crystalline pillars [35]. The picoindenter has several unique features that are crucial to this study. First, it includes a miniature capacitive load–displacement transducer permitting high-resolution measurements of load and displacement measurements (~0.3 μN in load, ~1 nm in displacement). In addition, rapid instrument response and data acquisition rates (the controller operating in a continuous loop and sampling data at 20 kHz) allows discrete flow events to be well resolved. The compression experiments were performed in two different control modes, i.e. displacement rate control that exhibits a greater sensitivity to transient load drops, and load rate control that has an advantage in evaluating transient displacement jumps. The displacement and/or load rate are programmed in such a way that a nominal strain rate of $\sim 10^{-2}\ s^{-1}$ is applied. A bending test was subsequently performed. In situ TEM observations are focused on the evolution of shear bands both spatially and temporally, whereas atomic scale observation is still quite limited even for the thinnest pillars, which is particularly due to the amorphous nature of the pillars. Post-mortem scanning electron microscopy (SEM) has been performed to aid the analysis.

3. Results

3.1. Evolution of shear bands under compression

Fig. 2 shows a sequence of frames grabbed from video that record the compression of a Cu-based pillar. The pillar has a relatively large tip diameter of 645 nm and was compressed under load rate control. The pillar shows elastic deformation followed by a jerky type deformation with transient shear banding events registered with displacement bursts in the displacement–load curve. The SBs 1 and 2 (marked in the images) initiated sequentially from the top

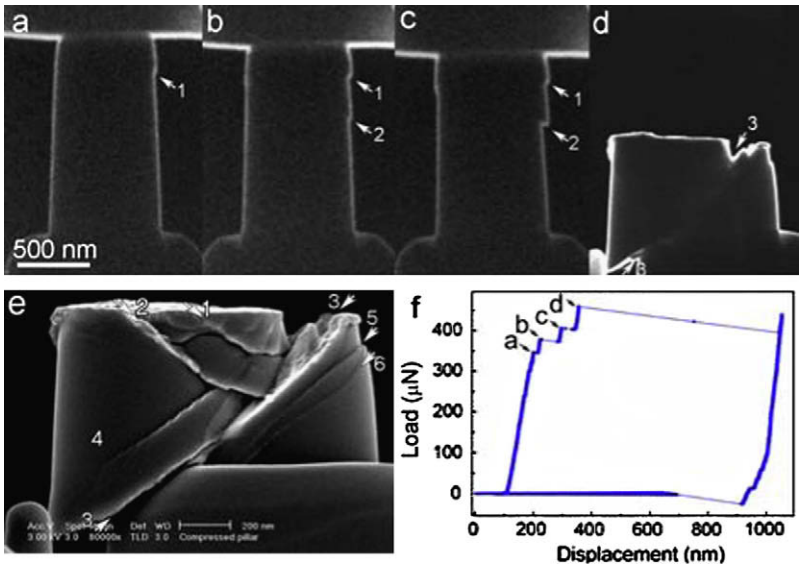

Fig. 2. Grabbed dark-filed TEM video frames recording the evolving deformation of Ø645 nm Cu-based MGs pillar compressed under load control: (a–d) morphologies immediately after jerky events *a*–*d* marked in the load–displacement curve in (f); (e) post-mortem SEM micrograph. The initiation of SBs 1 and 2 produced the jerky events *a* and *b*, respectively, whereas the subsequent growth/reactivation of the SB 2 causes the event *c*. The final large event *d* is associated with a major shear process, involving simultaneous operation of the major SB 3, and minor SBs 4–6 as indicated in image (e).

of the pillar, presumably due to combined effect of the slight tapering and the initial imperfect pillar–punch contact, causing the sequential appearance of bursts *a* and *b* in the curve. In contrast, the burst *c* is a result of a subsequent jerky type growth of the SB 2. Interestingly, the occurrence of the local SBs 1 and 2 does not seem to weaken the pillar. On the contrary, it enables the pillar to bear a higher load upon further loading due to the increase of the load-bearing diameter. With increasing load, the pillar finally deforms with a catastrophic major shear process. From the SEM image, this process is associated with the operation of multiple shear bands, i.e. the primary SB 3 carrying the majority of the shear displacement (strain) and a few neighboring secondary SBs (SBs 4–6). The secondary SBs with minor shear displacements may not traverse the pillar but die out gradually inside the pillar, e.g. the SB 4. The duration of the fast running process is very short (<0.04 s) and the sequence of the initiation of shear bands 3–6 cannot be resolved from the video frames and the load–displacement curve, indicating simultaneous occurrence of these multiple shear bands. The short duration, together with the large shear displacement (~690 nm in axial direction, and ~1 μm resolved to the shear plane), results in a rather high shear velocity (>25,000 nm s^{-1}).

Markedly, after the major shear process the pillar is not completely fractured. Upon further loading the load recovers quickly back to the previous value. Similar fracture tolerance and large engineering plastic strain have already been noticed at micrometer scale. It can be explained by an "extrinsic" size effect [17], since the critical shear offset at which failure happens (typically taken as 10–20 μm) in bulk MGs [36,37] cannot be reached in such small pillars.

Upon decreasing diameter, the deformation shows more pronounced intermittent characteristics. This is due either to more frequent initiation of new SBs or to repeated post-initiation growth (reactivation) of preexisting SBs in multiple steps. Fig. 3 shows frames snapped from a video recording the compression of a 440 nm tip-diameter pillar, which was compressed under displacement control and subjected to three loading–unloading cycles. While SBs 1 and 2 occurred successively causing load drop events *a* and *c* in the curve, respectively, SBs 3 and 4 are subsequently triggered, simultaneously causing a larger burst event *e*. Finally SBs 5 and 6 as well as a few minor SBs (see the post-mortem SEM) were triggered simultaneously during the last large burst *g*. Remarkably, none of these shear bands run over a long distance upon initiation. Instead, they are arrested after a small distance of propagation (~20 nm) and subsequently grow (or reactivate) intermittently in many steps, each of them carrying a limited shear offset. Therefore, a higher frequency of transient events in the load–displacement curve is detected. Compared to the predominant SB in the aforementioned thicker pillar the deformation here is more distributed into many events of shear bands initiation and subsequent propagation. This tendency increases upon decreasing diameter, as will be revealed by a statistical analysis in the following section.

The representative deformation morphologies of Cu-based pillars over the total investigated size range are shown in Fig. 4, and the representative engineering stress versus displacement curves are shown in Fig. 5. According to the SEM micrographs it is interesting to note that as the pillar diameter reduces from 650 to <100 nm, the apparent deformation mode shows a gradual transition from highly inhomogeneous to relatively homogeneous. A few well-developed major shear bands with sharp leading fronts at larger diameters in Fig. 4a–e are gradually transformed into

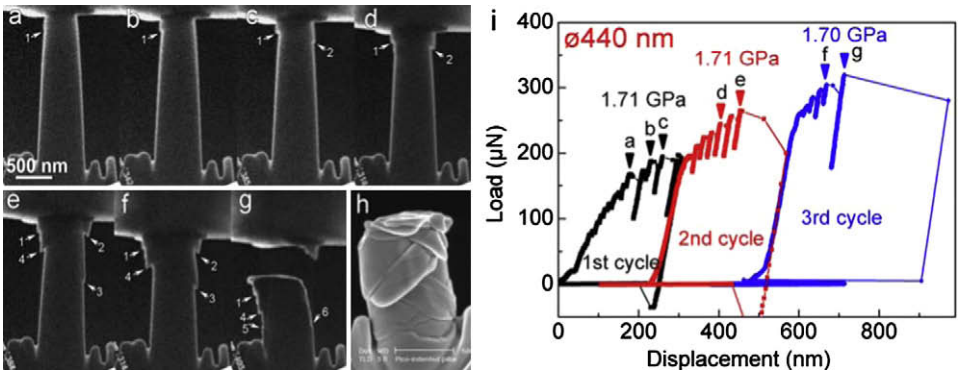

Fig. 3. Video frames recording the deformation of a Ø440 nm Cu-based MG pillar compressed under displacement control and subjected to three loading–unloading cycles. Frames (a–g) correspond, respectively to deformation structures immediately after jerky events *a*–*g* marked on the load–displacement curve in (i); (h) post-mortem SEM micrograph. The initiation of SBs 1 and 2 causes, respectively jerky events *a* and *c*. Subsequently, simultaneous initiation of shear bands 3 and 4 causes the larger event *e*. The other jumping events following the events *a*, *c* and *e* in the curve are associated respectively with intermittent growth (or repeated reactivation) of these preexisting SBs. Image frames (b) (d) and (f) highlight the markedly increased shear displacement of these SBs after the intermittent growth, respectively. The yield stresses measured in each loading cycle are also indicated in (i).

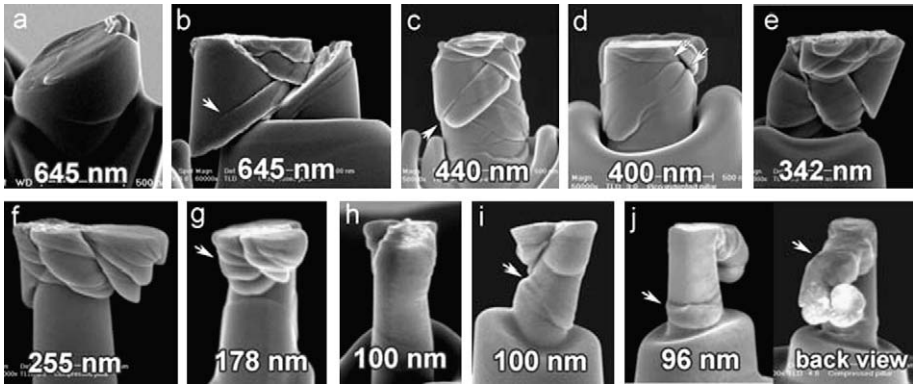

Fig. 4. SEM micrographs showing a global evolution of deformation morphologies of Cu-based MG pillars with tip diameters varying from 645 to 96 nm.

a larger number of diffuse shear processes with more rounded leading fronts and seemingly torsion-like morphologies (see the 255 and 178 nm pillars shown in Fig. 4f and g). This phenomenon becomes increasingly significant upon further decreasing pillar diameters down to ~100 nm. The inhomogeneity in the deformation of the 96 nm tip-diameter pillar is hardly detectable from the morphology (Fig. 4j), although the stress response curve still clearly records profuse shear banding events (Fig. 5d).

This tendency is also clear from the engineering stress versus displacement curves in Fig. 5. It can be seen that the frequency of bursts increases rapidly with decreasing pillar diameter. It indicates more frequently activated shear banding events, whereas the shear displacement/strain carried by individual shear banding events decreases fast, indicating suppression of shear band propagation. At the same time, a close-up examination of individual events (insets in Fig. 5) reveals that, with decreasing pillar diameter, the abrupt shear processes become increasingly gradual in thinner pillars. The shear displacement in thinner pillars proceeds more smoothly, while the stress decreases more steadily, in agreement with the observation of diffuse SBs.

These tendencies can be further described by a quantitative analysis of individual shear events versus diameter (Fig. 6). According to the data fitting, the fast increasing frequency f of bursts with decreasing diameter D follows roughly a power law decay of $f \propto D^{-1.3}$. The amplitude of the burst s can be expressed as $s_{\max} \propto D^{2.51}$ and $s_{av} \propto D^{1.2}$, where the subscripts denote the maximum burst and the average of rest bursts, respectively. The velocity of shear displacement jump (Fig. 6c) shows similar tendency as the amplitude and can be expressed as $v_{\max} \propto D^{2.60}$ and $v_{av} \propto D^{1.3}$, respectively.

From Fig. 6, at the smallest diameter of ~100 nm, the amplitude of the shear displacement jumps is very small (at the order of 10 nm), carrying a shear strain at the order of 1 assuming 10 nm shear band thickness according to TEM observations (see e.g. Ref. [38]). The propagation of the SBs takes a time lapse of tens of milliseconds, producing a very small shear velocity, less than 200 nm s^{-1}. A low propagation speed of SBs in small size MG pillars has also been noticed recently in another publication [14]. By compression measurements on MG pillars with effective diameters ranging between 200 and 300 nm, it is concluded [14] that "the shear displacement rate in each jerky motion was only a small fraction of 1 μm s^{-1}". At such a diameter our measurements would give a value around 100 nm s^{-1} and we can conclude that the velocity data match each

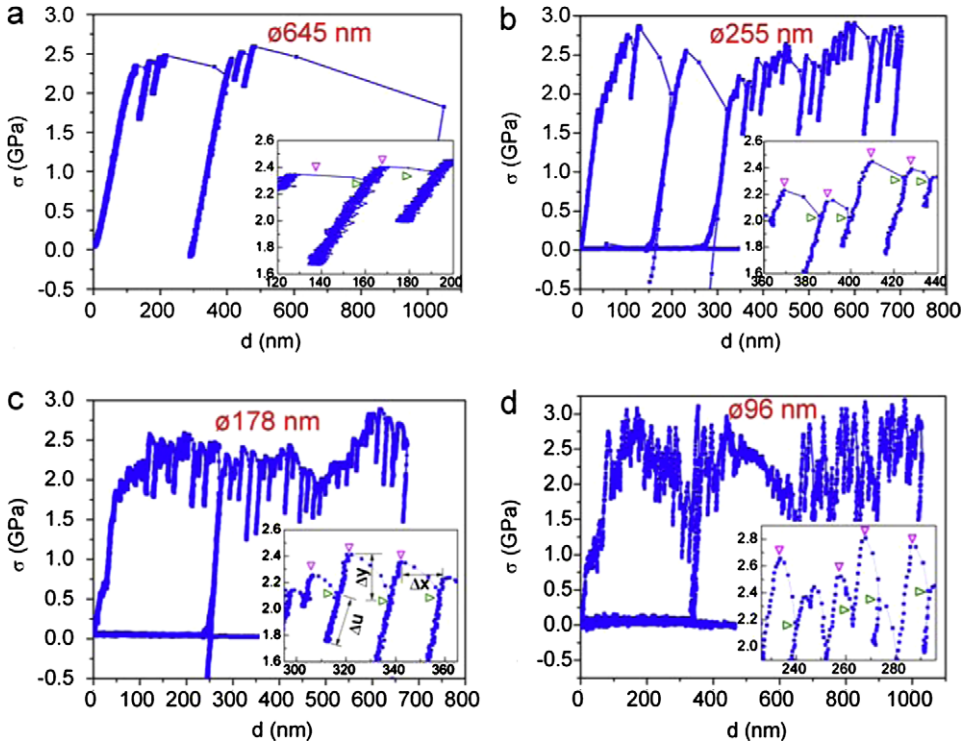

Fig. 5. Engineering stress σ versus displacement d curves of the Cu-based glass pillars under compression of tip diameters: (a) 645 nm, (b) 255 nm, (c) 178 nm and (d) 96 nm. The engineering stress is approximated by: $4P/[\pi(D+2u\tan\beta)^2]$ where P is the load, D the tip diameter, β the taper angle, and u the measured tip displacement. The insets are the enlarged plots showing the individual bursts with the start indicated by pink triangles and the end indicated by olive triangles. Δy denotes the stress drop and Δx the strain carried by an individual burst. Δu is post-burst elastic unloading due to transient withdrawal of indenter to match the predefined displacement rate. (For interpretation of the references to colour in this figure legend, the reader is referred to the web version of this article.)

other. This lower propagation speed here is in sharp contrast to the shear bands in unconstrained bulk MGs (BMGs), which propagate largely to tens of micrometers distance within a few nanoseconds to a couple of microseconds [39–42], resulting in an extremely high velocity, i.e. near the speed of sound. The relatively low speed indicates an incipient and immature nature of the shear bands in these small pillars compared to bulk. Also the acceleration and deceleration transients may contribute on average to a lower velocity compared to phenomena in bulk material.

3.2. Yield stress as a function of size

To accurately determine the yield stress, a test is normally interrupted at a certain stage to measure the effective load-bearing diameter, that is the minimum diameter at the purely elastically deformed region measured ahead of the most forefront SB. Together with the real time recorded load corresponding to this diameter, the procedure leads to an accurate determination of the yield stress (SB initiation stress). One of the examples is displayed in Fig. 3, with the measured values in each loading–unloading cycle indicated. It can be seen that, by measuring the instantaneous load-bearing diameter, the yield stresses recorded in different test cycles of the same pillar are quite reproducible.

Fig. 7 summarizes the measured values of the yield stress for a large number of micropillars, Cu-based and Zr-based, plotted as a function of effective pillar diameter. It turns out that there is essentially no diameter-dependence in the yield stress. This finding is in contrast to the recently reported dramatic size effects in increasing the yield stress of micrometer sized Mg-based and Zr-based glasses [14–16], but is closer to the latest studies on Pd-based amorphous alloys, which reported slight size effect but supposed this to be due to artifacts not excludable by the ex situ experiments [20,21].

As is well known, the high yield strength of metallic glass is due to the lack of an "easy" flow mechanism such as "dislocation sliding" in crystalline materials. As a consequence, in metallic glass one would not expect a "smaller is stronger" phenomenon observed, e.g. in nanocrystalline materials due to dislocation starvation mechanism [43,44]. The fracture strength (which is slightly higher than the yield strength) of BMGs is essentially controlled by interatomic bonding and has a roughly linear relationship with elastic modulus as $\sigma_f = 0.02E$ [3] or $\tau_y = 0.027G$ [45], where σ_f and τ_y are normal and shear fracture strength, and E and G are Young's modulus and shear modulus, respectively. This is still applicable to the present result of small volume pillars.

3.3. Evolution of shear bands under bending

The results so far dealing with microcompression have demonstrated a size-dependence in individual shear band-

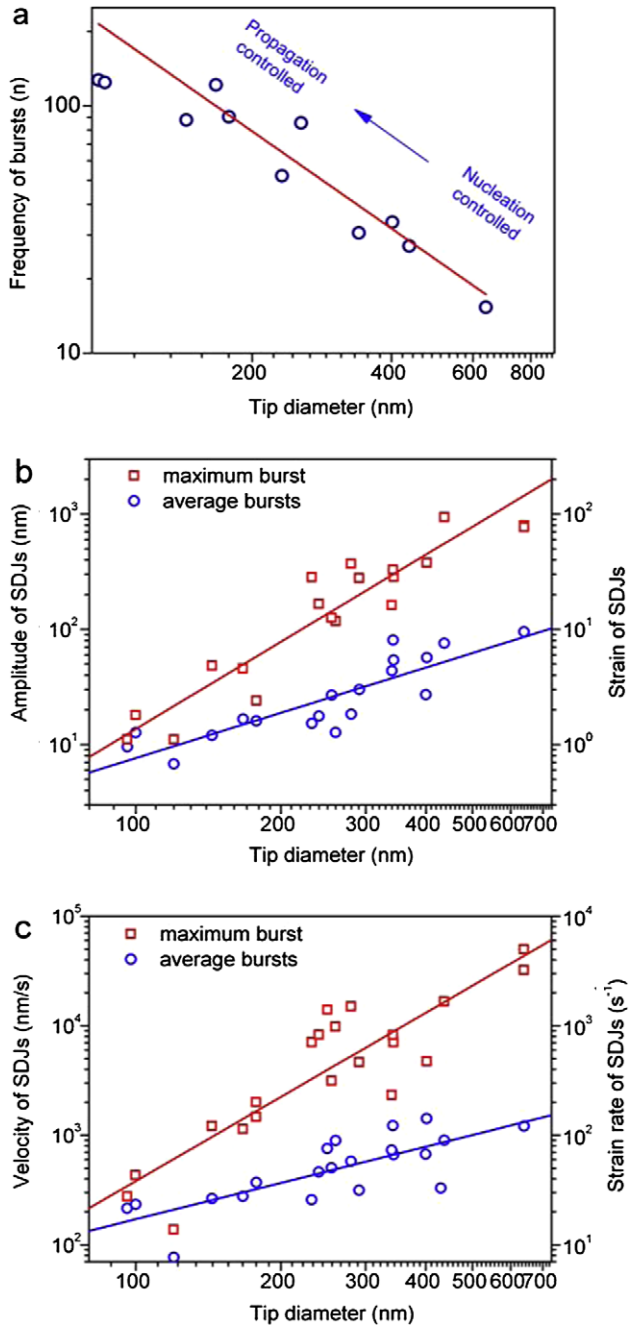

Fig. 6. Quantitative analysis of individual burst events as a function of pillar tip diameter: (a) frequency of bursts defined as the number of bursts per unit engineering strain; (b) amplitude and (c) velocity of shear displacement jumps (SDJs) transferred to 45° shear planes with the solid trend lines being power law fittings. The right axis reads the strain and strain rate of SDJs assuming 10 nm shear band thickness. Solid lines are power law fittings.

ing events, i.e. spatially from sharp to diffuse, or temporally from abrupt to gradual, with decreasing size. However, according to our analysis we have not clearly distinguished a homogeneous component in the deformation of the pillars subjected to compression. Although the thinnest pillar has apparently homogeneous deformation morphology, the deformation is still intermittent plastic flow accommo-

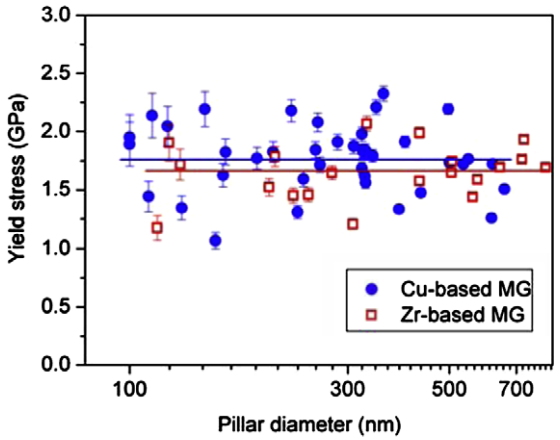

Fig. 7. Yield stress versus pillar diameter for both metallic glasses with trend lines indicated (the error bars indicate the uncertainties in stress due to column diameter determination).

dated by inhomogeneous shear banding. The apparent homogeneous flow is involved in the character of individual shear banding which is size-dependent. This is still the case, even with a diameter down to sub-100 nm scale, which is the experimentally accessible diameter limit for FIB milling. Nevertheless, we noticed that a deviation from uniaxial loading condition in the deformation of some extremely thin pillars may provide interesting hints of homogeneous flow. These sub-100 nm diameter pillars invariably have a rounded tip as a side product of FIB milling, while the initial deformation at the tip always flattens the rounded tips out by a bulging (mushrooming) effect, characteristic of homogeneous flow (Fig. 8). Presumably this phenomenon is promoted by a combined effect of the extremely small size and the local stress triaxiality arising from the rounded geometry. However, after this initial mushrooming stage, shear banding takes over. In an attempt to explore the possibility of a fully homogeneous deformation with decreasing size, we have designed microbending tests. It will be demonstrated that microbending tests have particular advantages since they minimize various artifacts and make the size effect more pronounced in an experimentally accessible regime.

There are a couple of practical difficulties in designing a standard microbending test inside a TEM due to the clamped-free boundary conditions. Simple deflection also suffers from the high stress concentration at the corner near the base. A practical solution that is proposed in this study is to intentionally introduce a small misalignment (3°) between the tip and the pillar. Considering the non-standard nature of the microbending test, a three-dimensional FEM (finite element modeling) approach was carried out to assist the stress–strain analysis by assuming an isotropic and ideally elastic–plastic material behavior. The results are shown in Fig. 9. It is seen that, when the stress on the compressive side just reaches the predefined yield point (1.7 GPa, see Fig. 7), deformation is already characterized by bending deformation with the left side under tension and right side under compression (neutral plane in green

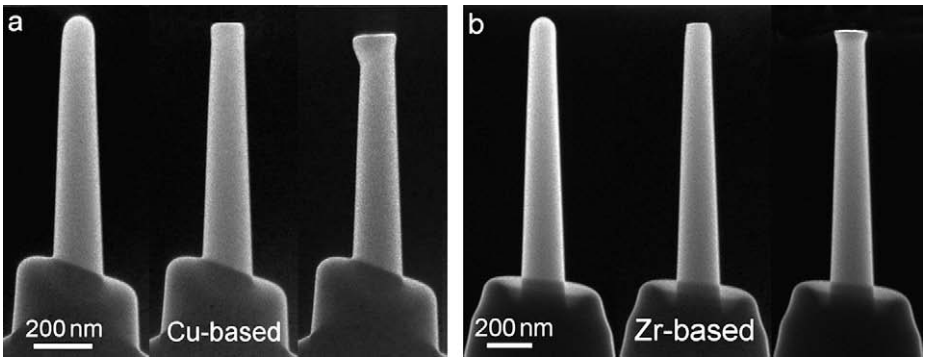

Fig. 8. Homogeneous deformation at the rounded top part of a Cu-based pillar with 100 nm tip diameter (a) and a Zr-based pillar with 116 nm tip diameter (b). The mushrooming bulge near the tip indicative of homogeneous deformation is prompted by the local multiaxial stress state.

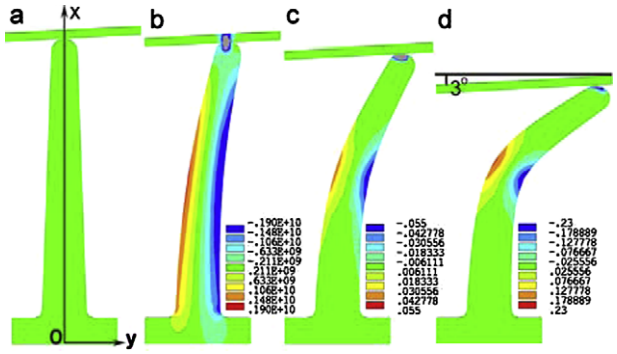

Fig. 9. Three-dimensional FEM of the bending test of a MG pillar with a 2° tapering. Bending is realized by applying a force 3° inclined to the pillar axis (normal to the contact surfaces). The MG is modeled as an isotopic and ideal elastic–plastic solid. (a) Solid model before deformation; (b) distribution of longitudinal stress when the stress under compression just reaches yield point; (c and d) showing evolving plastic strain distribution with bending.

in Fig. 9). The distribution of stress and strain is not fully symmetric yet, but becomes more symmetric with increasing tip displacement and finally close to symmetric bending. Importantly, the maximum deformation occurs around the region at half height (Fig. 9c and d), rather than near the tip-pillar contact (as is the case for monotonic compression) or at the base of the pillar (case in simple deflection). Thus, the complexity due to local stress concentrations is avoided and various related artifacts can be minimized. Notice that no details of shear banding or cracking can be observed from the FEM as isotropic plastic deformation is assumed and no microstructural features are involved.

3.4. Results of microbending: homogeneous versus inhomogeneous flow

Microbending tests carried out on pillars with relatively large diameters ($D > \sim 500$ nm) confirm that localized shear deformation (SBs) is still the dominant deformation mode, in agreement with the compression test. The deformation evolution of a 505 nm tip-diameter pillar is shown in Fig. 10. The shear displacements associated with SBs at

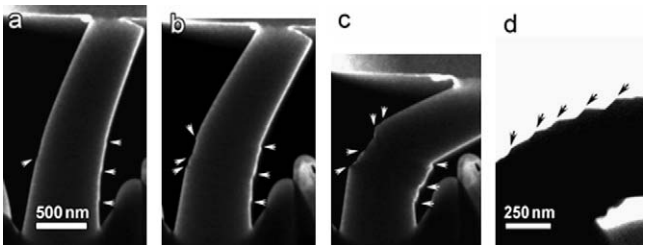

Fig. 10. In situ TEM observation of SB evolution (arrows annotated) during bending test of a 505 nm tip-diameter pillar (a–c). Another bent pillar of 480 nm tip diameter showing typical stair-like SBs at the surface is shown in (d).

the surface of the compressive side emerge almost simultaneously. Subsequently the first SB at the tensile side of the pillar nucleates, as shown in Fig. 10a. This sequence is consistent with the initial asymmetrical stress distribution due to a compression component overlapping with the bending. When deformation proceeds, more SBs are observed to nucleate at the tensile side and the shear offsets at both sides increase continuously. Fig 10d shows typical SBs with stair-like morphology due to shear offsets at the surface. Fracture is not observed in these pillars.

This observation of shear banding is similar to that observed in "bulk" MG plates hundreds of micrometers thickness [36,46,47]. Those plates showed multiple shear banding as the excessive development of one single SB is suppressed under bending. Ductility was found to increase with decreasing size [36,46,47], since the shear offsets necessary to cause fracture along a SB are hard to reach in a thin plate. This effect was satisfactorily explained as a purely geometric effect [36,46,47,37]. These understandings seem to remain valid for the pillars with the rather large diameters, since the deformation mechanism is not changed.

Micropillars with diameters decreasing to ~200 nm level show interesting new deformation mechanisms. One example of this is shown in Fig. 11. In agreement with the stress and strain distribution shown in Fig. 9, the middle part of this 185 nm tip-diameter pillar started to show pronounced deformation at the early stage of bending. Very interestingly, the deformation is rather homogeneous and not localized into a certain shear plane, and no detectable

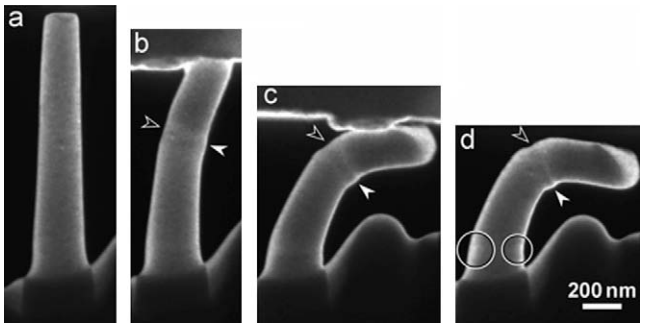

Fig. 11. A 185 nm tip-diameter pillar shown in (a) being bent at a rate of 20 nm s^{-1}, with images (b–d) acquired at different deformation intervals. The pillar shows at the middle height a bump under compression and concave/necking upon tension (indicated by solid and open white arrows, respectively), and fully homogeneous flow near the base, typical of ductile deformation.

sharp shear offsets associated with SBs were observed. Instead a small bump (indicated by solid white arrow) is observed at the compressive side and a small concave or necking (open arrow pointed) appeared in the tensile side at the position opposite to the bump. As deformation proceeds, the bump and necking become more pronounced, and the bump developed to a ridge on the corrugated surface under compression in Fig. 11c, typical of ductile deformation. At the lower part near the base the deformation is characterized by fully homogeneous flow without any detectable localization. When the load is removed, significant permanent deformation (e.g. up to 15% longitudinal strain near the base) accommodated by the homogeneous flow remains. Close-up inspection of the dark-field TEM image reveals some lighter contrast at the most deformed regions (arrows and circles marked), presumably due to stress-induced dilatation, or creation of flow defects known as free volume in shear transformation zones [9–11].

The effect of decreasing the pillar diameter from ~500 nm manifests itself by prohibiting any SBs from nucleating, and thus prompting the alternative deformation mechanism, i.e. fully homogeneous flow. Presumably, this is related to the extremely high stress gradient which cannot be reached at larger scale. Within the purely elastic regime, the longitudinal strain in an element within a vertical beam at a distance y from the neutral plane located at a position y_0 is expressed geometrically as $\varepsilon_{xx} = -(y - y_0)/\rho$, where ρ is the radius of curvature of the neutral plane. Approximately assuming $y_0 = 0$ (symmetric bending), the stress can be expressed as $\sigma_{xx} = -yE/\rho$, with E being the Young's modulus. Obviously σ_{xx} is the highest at $y = D/2$ (half diameter). As deformation proceeds, decreasing ρ builds up an increasing stress. Consequently, yielding or cracking occurs when σ at $y = D/2$ reaches a critical value σ_c at a minimum radius of curvature $\rho_c = -2\sigma_c/(ED)$. The stress can be expressed now as $\sigma_{xx} = -2\sigma_c \frac{y}{D}$. Obviously, σ_{xx} and stress gradient (σ_{xx}/y) scale inversely with diameter, and an extremely high stress gradient is expected at submicron diameter scale. With the presence of such a gradient, the high stress at one point at the surface may not be enough to initiate a SB, since the stress along the shear plane of the SB is decreasing sharply underneath the surface.

4. Discussion

4.1. Intrinsic size effects in the mechanical response

While the initiation of shear banding is controlled by the shear stress, the propagation of the shear band is governed by the stored elastic energy. Consider a deforming volume inside a pillar $V = L^3$ that accommodates an individual shear band, where L is linked to the diameter of the pillar D. The elastic strain energy accumulated in this volume is uV, where u is the elastic strain energy density, for uniaxial deformation $u = \sigma^2/(2E)$, σ being the stress. When a burst occurs under compression, the energy released is approximately $\Gamma = V(\sigma_i^2 - \sigma_{i+1}^2)/(2E)$, σ_i and σ_{i+1} are the stresses before and after the ith burst, i.e.

$$\Gamma_A = \frac{1}{4}\sqrt{2}\left(\sigma_i^2 - \sigma_{i+1}^2\right)\frac{L}{E} \tag{1}$$

where Γ_A is taken as the energy released per unit area of a 45° shear band. Obviously, Γ_A scales linearly with L. This helps to understand the modest deformation in smaller pillars. Rewriting the above equation gives:

$$\sigma_{i+1} = \sqrt{\sigma_i^2 - 2\sqrt{2}\frac{E\Gamma_A}{L}} \tag{2}$$

where σ_i is essentially equal to the size-independent yield stress of the MG pillars. The release of the same amount of energy per unit of area Γ in a thinner pillar results in a larger stress drop. This is indeed confirmed by a closer examination of stress drops shown in Fig. 5 (see the insets), via a comparison of individual bursts carrying similar displacements (strains), e.g. 20 nm, in pillars with different diameters. It is clear that the resultant stress drops less than 0.1 GPa in the Ø645 nm pillar is increasing continuously with decreasing diameters to more than 0.5 GPa in the Ø96 nm pillar. The experimentally observed stress drop is qualitatively consistent with the trend that can be predicted by Eq. (2). This is because the stress drop scales monotonically with the elastic energy that is transferred to unit area of SB. According to Eq. (2), a small volume needs a larger load drop to release the same amount of energy than released in a larger volume. Detailed evolution of the local stress field around the shear band needs further examination. A further quantitative prediction of the real value of the load drop is still rather difficult, due to lack of insights into the detailed physical processes that take place during shear banding.

Once the stress σ_{i+1} is lower than a critical value σ_c, a shear band ceases to propagate. σ_c reflects the strength of a shear band that is controlled by the amount of disorder. For shear bands carrying the same strain, σ_c can be considered as a constant. Due to larger stress drops in smaller diameter pillars, a shear band tends to stop. As a consequence, it

requires rebuilding of stress to reactivate the shear band or to initiate another one. This explains from a mechanics viewpoint the experimentally observed frequent arrest and re-initiation of SBs especially in thinner pillars. In a thick pillar, a propagating shear band has less opportunity to stop due to small load drop, and continuous propagation may further reduce the value of σ_c due to continuous free volume creation and also remarkable temperature increase [41,42], and consequently resulting in large bursts. In BMGs, the nucleation of a SB may directly lead to catastrophic failure. In this sense the deformation of larger specimens is essentially controlled by the nucleation of shear bands. With decreasing diameter, however, the frequent arrest of SBs indicated that the deformation becomes more likely controlled by SB propagation. However, it should be noted that this should be a gradual transition with decreasing size from bulk scale to nanoscale, and the biggest pillars in the present research is in fact already small compared to bulk specimen. This is why we still see moderate speed and multiple SBs.

Multiple shear banding had been confirmed by in situ observation shown in Figs. 2 and 3. In that case, the evolution of one single shear band is often coupled with that of another. Upon an attempt to fully resolve the evolution of one individual SB, a thinner pillar with tip diameter of 240 nm was particularly tested at a relatively low strain rate (one order lower than commonly used), as shown in Fig. 12. A number of jump events in the stress–response curve can be attributed to the intermittent growth (or repeated activation) of one major shear band traversing the pillar. This major SB is free of constraint at the leading front, but is frequently arrested, and reactivates only upon further increase in load. This observation can be well explained by, and is an extra support of, the micromechanical model proposed above.

To understand the appearance of the fully homogeneous flow, we extend the micromechanical model to the bending deformation. For bending we derive $U_{e-bend} = \sigma^2/(8E)$[1], with σ being the maximum value at $y = D/2$. Assuming that the energy is fully transferred to the SB, $U_{e(i+1)} = 0$ and consequently for compression and bending we have, respectively:

$$\Gamma_{A-uniax} = L\sqrt{2}\frac{\sigma_{uniax}^2}{4E} \tag{3}$$

$$\Gamma_{A-bend} = L\sqrt{2}\frac{\sigma_{bend}^2}{16E} \tag{4}$$

where σ_{uniax} and σ_{bend} are the maximum stress before shear banding under uniaxial and bending deformation, respectively. For both cases Γ_A scales linearly with L. Assuming σ_{bend} is close to σ_{uniax} (yield stress), for the same L, Eqs. (3) and (4) yield $\Gamma_{A-bend} = \Gamma_{A-uniax}/4$. To release the same amount of energy, it needs $L_{bend} = 4L_{uniax}$, with L_{bend} and L_{uniax} being the critical sizes necessary to nucleate a SB under bending and uniaxial deformation. This explains why the size effect, particularly the fully homogeneous flow which is unable to be observed even at sub-100 nm scale under compression, is shifted by microbending to a larger size regime above 200 nm, where experimental work is feasible. Based on the present bending tests it is possible to estimate the critical value Γ_{A-c} required to nucleate a shear band. Assuming a critical $L_{bend} = 220$ nm, using a size-independent yield stress of $\sigma_{bend} = 1.7$ GPa, and known $E = 100$ GPa, according to Eq. (4) $\Gamma_{A-c} = 0.56\ \mathrm{J\,m^{-2}}$. This is much smaller than the values of $10\ \mathrm{J\,m^{-2}}$ and $9\ \mathrm{J\,m^{-2}}$ used in a Pd-based [20] and a Zr-based [22] MG, respectively. Therefore it provides the reason why an expected switch in deformation mode from localization to homogeneity is not observed in Ref. [22], as the real value of the critical size may be much smaller than that used.

Based on the experiments and analysis so far, a deformation map can be introduced. If we assume $\sigma_{c-uniax}$ and σ_{c-bend} as critical stresses necessary to drive a SB (producing Γ_{A-c}) in a volume $\Omega = L^3$, after rewriting Eqs. (3) and (4), we arrive at

$$\sigma_{c-uniax} = 2^{3/4}\sqrt{\frac{E\Gamma_{A-c}}{L}} \tag{5}$$

$$\sigma_{c-bend} = 2^{7/4}\sqrt{\frac{E\Gamma_{A-c}}{L}} \tag{6}$$

Eq. (5) is similar to the one obtained in Ref. [20]. Obviously, the stress needed to drive a SB increases with decreasing characteristic length, and the stress required for bending is two times that of compression. As plotted in Fig. 13, deformation is characterized by shear banding and homogeneous flow under uniaxial deformation and microbending, respectively. This map clearly demonstrates the size-dependence of deformation modes and the relative threshold sizes of mode switch for compression and microbending, respectively.

This critical size for the transition of deformation modes from intermittent shear banding to homogenous flow may, in practice, be influenced by several aspects. The first factor is the material system and process-introduced defects. As in pillars of sputtered $Pd_{77}Si_{23}$, homogeneous deformation has been reported to emerge even at a diameter around 400 nm [20]. The second factor is the local stress state. The deviation from uniaxial state, like the initial local deformation at the rounded tip of the thin pillars shown in Fig. 8, and homogeneous bending in Fig. 11, has evidenced to suppress the shear band initiation. These observations indicate that the multiaxial loading at small sizes accelerates the inhomogeneous-to-homogeneous transition with decreasing diameters.

The physical description that emerges is the following: In MG pillars of randomly disordered structure, the yield strength is determined by cooperative shear motion of atomic clusters (also related to shear transformation zones (STZs) and flow defects [9–11,48]). In our view all sites

[1] According to basic formula from mechanics of materials: $\rho = EI/M$, $dU = (M^2/2EI)dx$, we get $dU_c = [\sigma_c/(rE)]^2(EI/2)dx$, since $I = \pi r^4/4$, $dU_c = (1/8)(\sigma_c^2/E)\pi r^2 dx = (1/8)(\sigma_c^2/E)dV$.

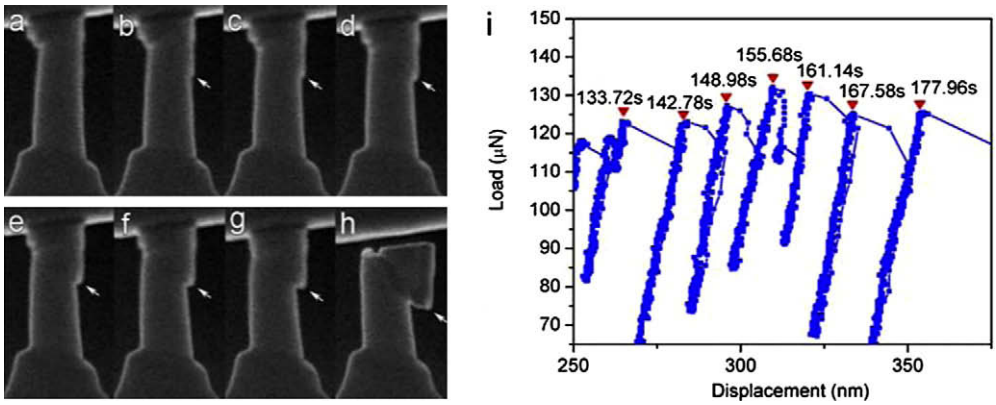

Fig. 12. Video snaps taken from the in situ TEM compression showing repeated interruption and re-initiation of an unconstrained shear band in a 240 nm tip-diameter pillar compressed at a programmed relatively low displacement rate of 2 nm s^{-1}. The unconstrained shear band, which is free at both ends, supporting 100% the applied load and growing intermittently, is associated with seven noticeable load drop events marked in plot (i). Images (b–h) highlight evolution of the shear band after each banding event marked in the load–displacement evolution curve in (i), where the exact time when each event happens is also annotated.

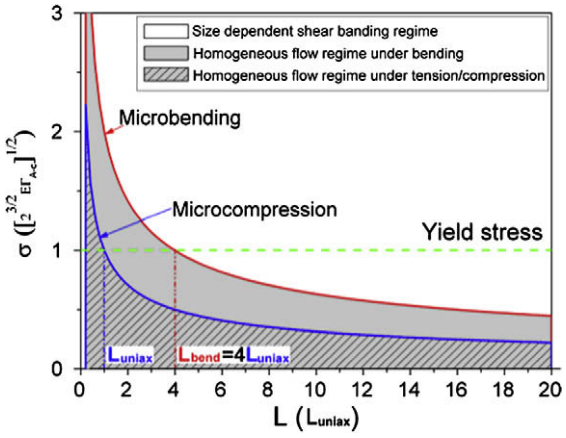

Fig. 13. A deformation map derived from Eqs. (3) and (4) plotting stress required to drive a shear band in a unit volume $\Omega = L^3$ as a function of L, illustrating a size dependence in deformation mode under bending and uniaxial deformation.

have equal probability of becoming a flow defect, the size of which depends on the applied stress. In our previous theoretical work [49–52] (based on molecular dynamics method) dealing with brittle fracture of randomly disordered system we derived the strength (taking into account the interaction between flaws):

$$\sigma_{fail} \propto (log\frac{h}{\xi})^{-1/\mu} \tag{7}$$

where ξ represents the correlation length within the samples of equal base and of a characteristic dimension h. The exponent μ depends on the dimensionality of the system and the interactions among the flow defects; theoretically it is equal to 4 in three-dimensional central force fields. Since $\xi_{\text{large sample}} > \xi_{\text{small sample}}$, a size-independent strength requires $\mu_{\text{small}} < \mu_{\text{large}}$. Theoretically upon decreasing size μ decreases from 4 to 1 [49–52], depending on the details of the interacting stress fields. Therefore, one expects that interactions among localized stress fields in a small size specimen may influence μ and also the mode of flow defect propagation. In a smaller volume the flow defects that are activated by the applied stress are statistically closer to each other whereas in a larger volume these flow defects are spatially uncorrelated at the onset of deformation. But the level of correlation does not affect the onset of deformation, i.e. the yield stress, as is confirmed in our experiments. If mechanical loading proceeds, the deformation zones in the vicinity of these flow defects will extend. In smaller pillars there exists a higher probability that they will interact, and the early connection of flow defects releases the energy earlier, giving rise to more frequent but smaller coalescence/burst events. If the size is small enough the intermittency will be shielded and the material will exhibit a fully homogeneous flow as was seen experimentally.

4.2. Possible extrinsic size effects in the mechanical response

Additional remarks that should be made concern the possibilities of "extrinsic" factors taking part in the size effects. One general concern about FIB milled pillars for mechanical tests is Ga^+ implantation, and the other one is the already mentioned tapering angle. Ga^+ implantation has been recognized to have only a minor effect on the deformation behavior of submicrometer samples, especially of amorphous materials which are radiation tolerant [20]. A FIB introduced disordered surface layer of 3–4 nm thickness [19] and containing less than 1 at.% Ga concentration [20] is unlikely to have remarkable effects on the behavior of intrinsically disordered metallic glasses. The tapering angle of 2–3.5° is rather small compared to the 7–15° in other studies which were capable of producing MG pillars with diameters down to submicrometer scale [14,18,20,21,23]. In addition, the in situ TEM observation correlates the structure evolution and load response effectively, which further minimizes possible artifacts. Although the slight tapering still causes the deformation starting from the top and proceeding towards the base, a SB gener-

ally traverses through the pillar without constraint at either the leading or the rear front. Nevertheless, the unconstrained SBs do not run away largely but develop intermittently, with the energy released and re-accumulated repeatedly in the limited volume, indicating intrinsic effects. Moreover, with the designed bending test the limitations of the compression test were circumvented and consequently a robust size effect was appeared.

Another influencing factor is the effective strain rate. As reported from nanoindentation [53–56] and uniaxial deformation [57] of BMGs, high strain rate may lead to apparent homogenous deformation, however, which is obvious only when the strain rate scales over 3–4 orders of magnitude. In this study, all compression is controlled at the same nominal strain rate of $\sim 10^{-2}\,s^{-1}$, which is unlikely to cause noticeable effects of strain rate on the deformation mode. An exception is the 240 nm pillar compressed at a relatively lower rate (Fig. 12), which, however, shows frequent arrest of the shear band instead of fast and large propagation preferred by a low strain rate, further pointing at an intrinsic size effect.

5. Conclusions

Compression tests of MG pillars, having diameters ranging from 93 to 645 nm, show predominant inhomogeneous and intermittent plastic flow characterized by shear banding events. It is concluded that the deformation is defect-nucleation-controlled in larger pillars but becomes propagation-controlled in smaller pillars. A micromechanical model is proposed which supports the conclusion that suppression of shear band propagation is an intrinsic size effect. Interestingly, the yield stress is essentially size-independent in comparison to crystalline materials. A transition to a fully homogeneous flow is not observed in microcompression but has been detected in microbending experiments. The micromechanical model is extended to microbending and the transition to a fully homogeneous deformation is explained. Based on the model description, a deformation map is brought forward and a physical picture regarding micro-/nano-scale shear localization process is provided, suggesting that the spatiotemporal correlations between interacting stress fields of flow defects play a decisive role in the size-dependent mechanical response of MG.

Acknowledgements

We acknowledge financial support from M2i (Materials Innovation Institute) and FOM-Utrecht, The Netherlands.

References

[1] Klement W, Willens RH, Duwez P. Nature 1960;187:869.
[2] Greer AL, Ma E. MRS Bull 2007;32:611.
[3] Inoue A. Acta Mater 2000;48:279.
[4] Schuh CA, Hufnagel TC, Ramamurty U. Acta Mater 2007;55:4067.
[5] Matthews DTA, Ocelik V, Bronsveld PM, De Hosson JTM. Acta Mater 2008;56:1762.
[6] Inoue A, Zhang T, Masumoto T. Mater Trans JIM 1990;31:177.
[7] Peker A, Johnson WL. Appl Phys Lett 1993;63:2342.
[8] Zhang ZF, Eckert J, Schultz L. Acta Mater 2003;51:1167.
[9] Spaepen FA. Acta Metall 1977;25:407.
[10] Argon AS. Acta Metall 1979;27:47.
[11] Falk ML, Langer JS. Phys Rev E 1998;57:7192.
[12] Schuh CA, Lund AC. Nat Mater 2003;2:449.
[13] Guo H, Yan PF, Wang YB, Tan J, Zhang ZF, Sui ML, et al. Nat Mater 2007;6:735.
[14] Shan ZW, Li J, Cheng YQ, Minor AM, Syed Asif SA, Warren OL, et al. Phys Rev B 2008;77:155419.
[15] Zheng Q, Cheng S, Strader JH, Ma E, Xu J. Scripta Mater 2007;56:161.
[16] Lee CJ, Huang JC, Nieh TG. Appl Phys Lett 2007;91:161913.
[17] Cheng S, Wang XL, Choo H, Liaw PK. Appl Phys Lett 2007;91:201917.
[18] Schuster BE, Wei Q, Ervin MH, Hruszkewycz SQ, Miller MK, Hufnagel TC, et al. Scripta Mater 2007;57:517.
[19] Lai YH, Lee CJ, Cheng YT, Chou HS, Chen HM, Du XH, et al. Scripta Mater 2008;58:890.
[20] Volkert CA, Donohue A, Spaepen F. J Appl Phys 2008;103:083539.
[21] Schuster BE, Wei Q, Hufnagel TC, Ramesh KT. Acta Mater 2008;56:5091.
[22] Dubach A, Raghavan R, Löffler JF, Michler J, Ramamurty U. Scripta Mater 2009;60:567.
[23] Wu XL, Guo YZ, Wei Q, Wang WH. Acta Mater 2008;57:3562.
[24] Hofmann DC, Suh JY, Wiest A, Duan G, Lind ML, Demetriou MD, et al. Nature 2008;451:1085.
[25] Hofmann DC, Suh JY, Wiest A, Lind ML, Demetriou MD, Johnson WL. Proc Natl Acad Sci 2008;105:21036.
[26] Launey ME, Hofmann DC, Johnson WL, Ritchie RO. Proc Natl Acad Sci 2009;106:4986.
[27] Hays CC, Kim CP, Johnson WL. Phys Rev Lett 2000;84:2901.
[28] Donohue A, Spaepen F. Appl Phys Lett 2007;91:241905.
[29] Wang YM, Li J, Hamza AV, Barbee Jr TW. Proc Natl Acad Sci 2007;104:11155.
[30] Ashby MF, Greer AL. Scripta Mater 2006;54:321.
[31] Soer WA, De Hosson JTM, Minor AM, Morris Jr JW, Stach EA. Acta Mater 2004;52:5783.
[32] Soer WA, De Hosson JTM, Minor AM, Shan ZW, Syed Asif SA, Warren OL. Appl Phys Lett 2007;90:181924.
[33] De Hosson JTM, Soer WA, Minor AM, Shan ZW, Stach EA, Syed Asif SA, et al. J Mater Sci 2006;41:7704.
[34] Minor AM, Syed Asif SA, Shan ZW, Stach EA, Cyrankowski E, Wyrobek TJ, et al. Nat Mater 2006;5:697.
[35] Shan ZW, Mishra RK, Syed Asif SA, Warren OL, Minor AM. Nat Mater 2007;7:115.
[36] Conner RD, Johnson WL, Paton NE, Nix WD. J Appl Phys 2003;94:904.
[37] Ravichandran G, Molinari A. Acta Mater 2005;53:4087.
[38] Zhang Y, Greer AL. Appl Phys Lett 2006;89:071907.
[39] Zhang HW, Maiti S, Subhash G. J Mech Phys Solids 2008;56:2171.
[40] Yang B, Morrison ML, Liaw PK, Buchanan RA, Wang G, Liu CT, et al. Appl Phys Lett 2005;86:141904.
[41] Lewandowski JJ, Greer AL. Nat Mater 2006;5:15–8.
[42] Spaepen F. Nat Mater 2006;5:7.
[43] Greer JR, Oliver WC, Nix WD. Acta Mater 2005;53:1821.
[44] Uchic MD, Dimiduk DM, Florando JN, Nix WD. Science 2004;305:986.
[45] Johnson WL, Samwer KA. Phys Rev Lett 2005;95:195501.
[46] Schroers J, Johnson WL. Phys Rev Lett 2004;93:255506.
[47] Conner RD, Li Y, Nix WD, Johnson WL. Acta Mater 2004;52:2429.
[48] Srolovitz D, Vitek V, Egami T. Acta Metall 1983;31:335.
[49] Chung JW, De Hosson JTM. Phys Rev B 2002;66:064206.
[50] Chung JW, De Hosson JTM, van der Giessen E. Phys Rev B 2002;65:094104.
[51] Chung JW, De Hosson JTM, van der Giessen E. Phys Rev B 2001;64:64202.

[52] Chung JW. De Hosson JTM, van der Giessen E. Phys Rev B 1996;54:15094.
[53] Burgess T, Laws KJ, Ferry M. Acta Mater 2008;56:4829.
[54] Schuh CA, Lund AC, Nieh TG. Acta Mater 2004;52:5879.
[55] Yang B, Nieh TG. Acta Mater 2007;55:295.
[56] Song SX, Jang JSC, Nieh TG. Intermetallics 2008;16:676.
[57] Mukai T, Nieh TG, Kawamura Y, Inoue A, Higashi K. Intermetallics 2002;10:1071.